Climate-adaptive prediction of wind erosion risks for earthen heritage under multi-scenario futures

Climate Risk Management 51 (2026) 100763

Contents lists available at ScienceDirect

Climate Risk Management

journal homepage: www.elsevier.com/locate/crm

Climate-adaptive prediction of wind erosion risks for earthen heritage under multi-scenario futures

Qiong Wang [a], Jun Xiao [a], Anrong Dang [a,*], Xiuyun Xu [b], Jingxiong Huang [a], Ruihua Zhang [a]

[a] Department of Urban Planning and Design, School of Architecture, Tsinghua University, No. 30, Shuangqing Road, Haidian District, Beijing 100084, China

[b] Beijing Vitspace Technology Co., Ltd., Keyuan Road No. 3, Economic Development Zone, Daxing District, Beijing 100176, China

ARTICLE INFO

Keywords:
Cultural heritage conservation
Earthen heritage
Wind erosion
Climate change
Risk assessment
computational fluid dynamics (CFD)

ABSTRACT

Earthen heritage sites are vital components of global cultural assets, yet face intensifying wind erosion driven by more frequent extreme wind events. Accurate erosion prediction is critical to preserve structural integrity and guide climate-adaptive management under UNESCO's climate action framework. However, current methods rely on simplified geometry models or limited wind simulations, producing insufficient spatial resolution and overlooking differential mass loss among components. Temporally, projections based on linear extrapolation from typical years neglect long-term, non-stationary trends. This study developed an integrated prediction framework combining centimeter-scale LiDAR modeling, high-resolution computational fluid dynamics (CFD), and CMIP6 multi-scenario climate data. Applied to the representative Chinese earthen heritage site Xixia Imperial Tombs, the framework produces site-wide risk maps and identifies localized high-risk zones. Results quantify nonlinear erosion responses to wind speed gradients, extending conventional initiation thresholds with acceleration inflection points. Temporal resampling refines wind-speed resolution, producing annual projections of cumulative erosion metrics (mass, depth, volume) through 2100 under SSP2–4.5 and SSP5–8.5 scenarios. The intermediate SSP2–4.5 pathway shows higher interannual variability and greater mean cumulative erosion than the high-forcing SSP5–8.5 scenario, indicating elevated long-term degradation risk under moderate climate forcing. Both scenarios displayed wide uncertainty ranges, suggesting a substantial likelihood of extreme erosion outcomes beyond mean projections. By integrating high-precision simulation with scenario-sensitive climate data, this framework advances predictive modeling of climate-driven hazards in the built environment and supports resilient planning and conservation of earthen heritage in arid regions.

1. Introduction

Earthen heritage sites constitute vital cultural and economic assets worldwide. More than 150 UNESCO World Heritage properties are built partially or entirely from earth, accounting for over 10 % of all inscribed sites (David Gandreau and Leticia Delboy, 2012; UNESCO, 2013). Globally, 15–17 % of the population resides in earthen buildings (Mariana Correia, 2016). China hosts one of the

* Corresponding author.
E-mail address: danrong@mail.tsinghua.edu.cn (A. Dang).

https://doi.org/10.1016/j.crm.2025.100763
Received 28 September 2025; Received in revised form 2 November 2025; Accepted 6 November 2025
Available online 20 November 2025

Nomenclature

List of symbols

H	height (m)
Y_d	cumulative mass fraction
N	spread parameter
S_G	CFD computational domain (m^2)
d	particle diameter of rammed earth in the case
Vi	daily average wind speed
V_D	the daily average wind speed
E_{Vi}	erosion rate intensity (kg/m^2-s) on a unit mesh cell of the heritage
$P_{Vi,D}$	the percentage of hours per day during which the wind speed exceeded the erosion-initiation threshold (8 m/s)
$P_{S,D}$, $P_{N,D}$	Probability (%) of south wind (S) and north wind (N) occurring on the Dth day, statistically derived from wind rose data.
Q_y	annual erosion spatial intensity for a unit mesh cell in year y (kg/m^2)
M_y	total annual erosion mass in year y (kg)

largest concentrations of such heritage, with 1,251 nationally protected earthen sites recorded in 2019. However, many are located in ecologically vulnerable arid and semi-arid regions, where conservation is particularly challenging. About 25 % of earthen sites appear on the List of World Heritage in Danger (World Heritage Centre, 2021b), continuously exposed to multiple threats, including wind and rain erosion, flooding, earthquakes, and anthropogenic influences.

In arid zones, high-frequency wind events are major drivers of rammed earth deterioration (Richards et al., 2020c). High-speed clean winds polish and loosen surface materials, while sand-laden winds accelerate surface pitting. Rainfall exacerbates these processes by weakening cohesion and promoting structural failure (Richards et al., 2019; Richards et al., 2020c). Climate change is expected to intensify extreme wind events, thus accelerating erosion and vibrational stress (UNESCO, 2008). Already, one-sixth of global cultural heritage sites, including earthen heritages, have shown adverse climate impacts (World Heritage Centre, 2021a).

To mitigate climate impacts, quantifying wind erosion under diverse wind conditions is fundamental to safeguarding the integrity

Table 1
Review of representative studies on wind erosion of earthen heritage sites.

Reference	Case	Scale	Focus	Method	Conditions	Erosion Metrics	Span
(Z. Guo et al., 2024)	Jiaohe Ruins, China	9 wall diagrams	Surface peeling	GIS, SMO	–-	Wall-to-surface area ratio	–-
(Shao et al., 2013)		5 soil samples.	Soil erosion modulus	Wind tunnel, formulas	Wind speed × particle	Erosion modulus (kg/m^2·h)	–-
(Richards et al., 2019; Richards et al., 2020c)	Suoyang Ancient City, China	9 wall scan images.	Surface change	Field testing, laser scanning	Clear wind / sand-laden wind / rainfall × 3 speeds	Max. erosion depth (mm)	–-
(Z. Guo et al., 2023)		6 areas on 1 wall	Surface change	Laser scanning	–-	Surface roughness	–-
(Chen et al., 2025)		Rectangular wall (70 m)	Gravel transport visualization	CFD	Sand-laden wind (monodisperse), 4 speeds	–-	–-
(Chen et al., 2023)		Inner city (1.0 km^2)	Deposits deflation	SBAS-InSAR	–-	Erosion rate (mm/yr)	7 years
(Q. Guo et al., 2025)		4 rammed-earth walls	Cross-sectional erosion depth	Field tests, numerical sim., 3D scanning	–-	Erosion depth (mm)	Past 47 months
(Richards et al., 2020a; Richards et al., 2020b)		2 walls (50 m;10 m)	3 wind erosion risks types	ViSTA-HD	Sand-laden wind × 3	Unit risk ratio	100 years on
(Chen et al., 2020)	Jiayuguan Pass, China	Test block (7.07^3 cm^3)	Wind speed vs. erosion rate	Wind tunne	Sand-laden wind × 4	Erosion rate (g/min)	–-
(Qu et al., 1994)	NA	Frozen/ unfrozen soil	Testing reinforcement	Wind tunne	Sand-laden wind × 6	Erosion modulus (kg/m^2·h)	–-
(Pineda & Iranzo, 2017)	Baelo Claudia, Spain	10 columns	Annual erosion rate	CFD	2 wind directions × 3 speeds	Erosion rate (kg/yr)	50–100 years

and authenticity of earthen cultural heritage (UNESCO, 2021). Such assessments clarify erosion-response mechanisms, identify threshold wind speeds, and provide a basis for micro-meteorological monitoring and early warning. Also, quantifying spatial differences in surface wind erosion rates supports differentiated conservation measures, as 3D morphology alters local airflow and prevailing winds create distinct erosion intensities across orientations. However, because wind erosion progresses slowly and is often imperceptible (Orr et al., 2021), trend analysis over long timescales is required (Sesana et al., 2021). When coupled with climate models, such analysis can project multiple future erosion pathways.

Despite substantial progress in understanding climate-induced deterioration of earthen heritage, two major methodological gaps remain unresolved: (a) the lack of high-resolution spatial erosion mapping and (b) the lack of temporally dynamic, climate-sensitive prediction. Spatially, existing methods remain inadequate for delineating fine-grained spatial variability under comprehensive wind conditions at the site scale (Table 1). Wind-tunnel tests yield erosion depth for isolated walls or soil blocks (Qu et al., 1994; Yan et al., 2009) but fail to represent whole-site morphology and its effects on wind acceleration. Although computational fluid dynamics (CFD) simulations can resolve wind fields and shear stresses (Ashraf S. Hussein and Hisham El-Shishiny, 2009), they rarely link flow patterns to erosion rates or mass-loss indicators. Most simulations consider only a few representative wind conditions (Chen et al., 2020; Qu et al., 1994) without incorporating a comprehensive assessment across the full range of historical wind regimes (Pineda and Iranzo, 2017).

Temporally, current approaches rely on static or extrapolated wind regimes, ignoring the non-stationary, scenario-dependent nature of future climates. Existing methods for extending historical wind data into future predictions generally fall into two types (Table 1): deriving future wind-speed ranges from literature and applying probability density functions to simulate century-scale erosion (Richards et al., 2020a), or assuming constant wind regimes and extrapolating typical-year erosion linearly with CFD (Pineda and Iranzo, 2017). Both overlook temporal variability and rely on single scenarios. Although CMIP6 projections incorporate multiple emission pathways and socioeconomic trajectories and have been widely applied to near-surface wind prediction (Jiang et al., 2010; Long et al., 2021; Pineda and Iranzo, 2017), their coarse temporal resolution fails to capture transient high-wind events that drive erosion, limiting direct application to archaeological sites. Addressing temporal downscaling is therefore essential for robust long-term projections.

Consequently, an integrated framework that links high-resolution site-scale simulations with multi-scenario climate projections is urgently needed. This study presents such a framework by coupling site-scale CFD simulations with CMIP6 multi-scenario climate projections to address current methodological gaps through their complementary strengths. This integration framework is designed to achieve the following objectives: (1) establishing a centimeter-scale CFD modeling system capable of simulating site-level wind erosion under complex morphologies and across full wind-speed gradients; (2) integrating CMIP6 climate drivers for century-scale predictions of erosion dynamics; (3) identifying nonlinear erosion thresholds and spatial risk hotspots; and (4) providing quantitative tools to support the predictive conservation and climate-adaptive management of earthen heritage sites.

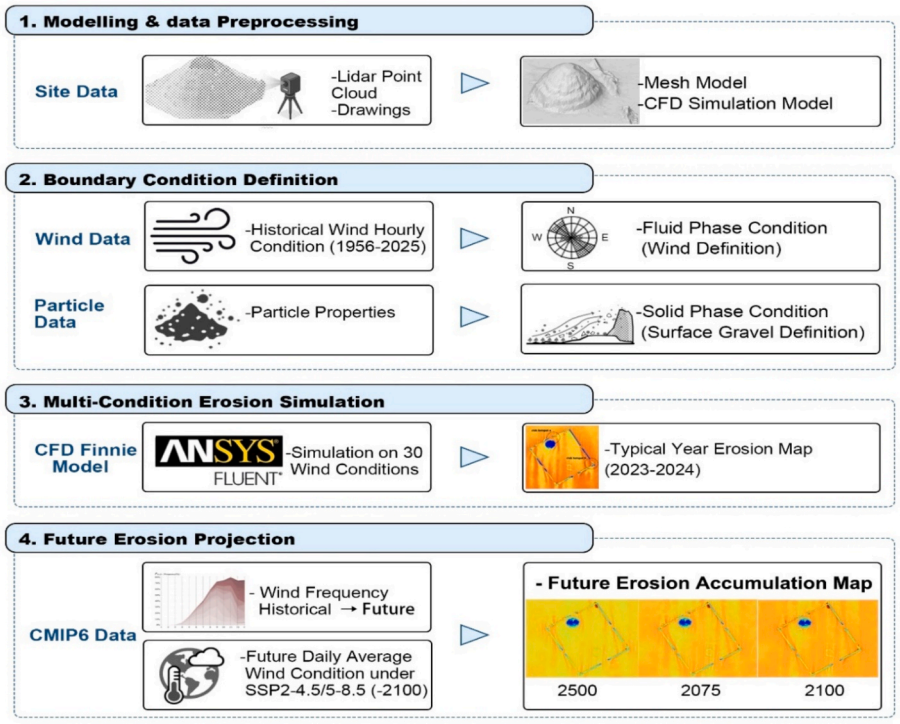

Fig. 1. Research workflow.

2. Method

To simulate and project wind erosion of earthen heritage under climate change, a four-step framework was developed (Fig. 1). First, high-resolution laser scanning and archaeological surveys generated precise site-scale geometries, followed by mesh generation for CFD analysis. Second, wind flow conditions, surface particle characteristics, and rammed-earth material properties were defined based on literature, and multiple wind scenarios were established using historical meteorological records. Historical near-surface wind-speed records were analyzed to calculate the frequency of extreme wind events in daily-mean wind-speed bins. Assuming the occurrence probability $P_{Vi,D}$ for an extreme wind level Vi on day D with a specific daily-mean velocity remains stable in the future, the occurrence and duration of extreme conditions in a future period could be estimated. Third, several boundary conditions Vi of the extreme wind scenarios above were simulated by CFD, considering threshold friction velocity and prevailing wind direction. The spatial distributions of erosion E_{Vi} were collected. Finally, after CMIP6 wind datasets were incorporated, the spatial and summarized outputs of CFD simulation were stacked by the future occurrence probability of their extreme wind boundary conditions to total erosion mass M under multiple climate scenarios (Eq. (1)).

$$M = \sum_{t}\sum_{Vi} E_{Vi}P(Vi,D)\Delta t \tag{1}$$

2.1. Case modeling and mesh generation

Approximately half of China's earthen heritage sites are located in arid and semi-arid northwestern regions (SUN et al., 2022), among which the Xixia Mausoleum represents a typical case (Fig. 2). As the largest, highest-ranking, and best-preserved archaeological site from the Western Xia period (11th–13th centuries), the mausoleum is situated at the eastern foothills of the Helan Mountains in Yinchuan, Ningxia, covering nearly 40 km^2 and comprising 9 imperial tombs and 271 ancillary burial sites. Owing to its exceptional authenticity and integrity, it was inscribed on the UNESCO World Heritage List in 2025 (UNESCO World Heritage Centre, 2025). Among these, Tomb No. 3 stands as the most well-preserved imperial tomb in its original form, offering outstanding research value (Institute of Architectural History, China Architecture Design & Research Group et al., 2020). Despite preventive measures such as anchoring supports and anti-weathering chemical treatments (Wang et al., 2002), the entity continues to suffer surface abrasion, flaking, and weathering-induced undermining, with wall collapses previously reaching 189.1 m, accounting for 27.8 % of the total length (Lin et al., 2009; Wang et al., 2002). Consequently, this study selected Tomb No. 3 as the research subject for a quantitative assessment of its wind erosion risk.

Given the lack of measured data correlating wind conditions with erosion rates, CFD simulation was employed as the primary investigative method. High-resolution LiDAR point cloud data of the Mausoleum No. 3 tomb platform were collected, totaling 324 million points with a measurement error of < 1 cm, provided by VitSpace Inc. Archaeological survey drawings of the entire mausoleum complex with detailed dimensional parameters were also obtained, and key material parameters (Appendix A) were collected from publicly accessible databases including CNKI and Web of Science.

An integrated multi-software workflow was implemented to develop a refined 3D model (Fig. 3). The point cloud data were processed using CloudCompare and MeshLab for coordinate correction, noise reduction, and octree-based downsampling to balance detail with computational efficiency. The walls and microtopography of the case were reconstructed in SketchUp. These model components were then merged, overlapping faces were removed, and topological optimization was performed in ANSYS SpaceClaim to generate a watertight model suitable for CFD simulation.

The CFD computational domain was configured according to the Architectural Institute of Japan (AIJ) guidelines, set to 20H × 16H × 6H (H = 21 m; inlet: 8H, outlet: 12H), resulting in a total volume of 17,781,120 m^3. A dense mesh was generated within this domain to enhance simulation accuracy. Mesh quality inspection indicated an average cell quality > 0.75, maximum skewness of 0.85, and maximum orthogonality of 1.0, confirming that the mesh quality was medium to high and suitable for subsequent numerical

Fig. 2. Case study overview. (a) Distribution map of the Xixia Imperial Tombs earthen heritage complex; (b) Plan of Xixia Imperial No. 3 tomb; (c)-(e) Current surface erosion features of No. 3 tomb.

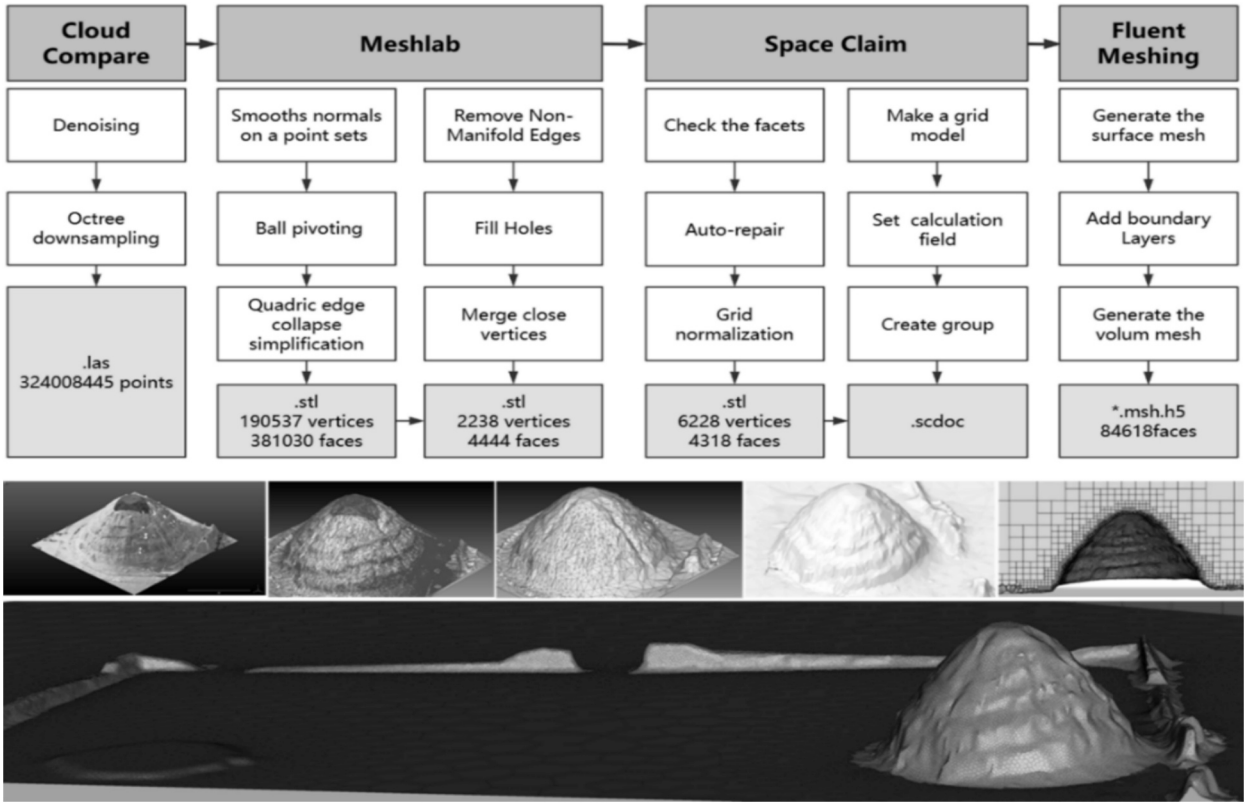

Fig. 3. CFD Modelling workflow: compliance with Japanese AIJ standards.

Table 2
Comparative Summary of Wind Erosion Models.

Model	Input	Output	Wind Type	Soil Type	Study Object	Inference Method
Texas Erosion Analysis Model (Gregory et al., 2004)	Surface cover factor, non-cohesive particle movement rate, shear velocity, critical shear velocity, soil shear strength, shear angle, bare surface length	Soil movement rate per unit time	Sand-laden wind	Field plot soil	California dust storms	Computer simulation, Wind tunnel experiment
Small Watershed Soil Wind Erosion Statistical Model (Dong, 1998)	Wind speed, air humidity, soil particle size, soil hardness, vegetation coverage, surface breakage rate, slope	Soil loss rate per unit time	Clean wind	Watershed soil	Liudaogou, Shenmu County, China	Wind tunnel experiment
Loess Sandy Soil Wind Erosion Regression Equation (Weinan Chen et al., 1996)	Actual wind speed, threshold wind speed	Wind erosion modulus per m^2 per unit time	Clean wind	Loess sandy soil	Northern Loess Plateau, China	Wind tunnel experiment
Raw Soil Wind Erosion Formula (Rong et al., 2004)	Moisture content, wind speed	Wind erosion amount per meter per unit time	Clean wind	Construction sand and raw soil	Unspecified	Field measurement with custom wind tunnels
Single-Factor Regression Equation for Earthen Heritage Wind Erosion (Qu et al., 1994)	Erosion area, duration, wind speed	Wind erosion modulus per m^2 per unit time	Clean and sand-laden wind	Northwestern earthen heritage soil	Shandan Ming Great Wall and Dunhuang Mogao Grottoes, China	Wind tunnel experiment, Mathematical derivation
CFD Finnie Erosion Model (Pineda & Iranzo, 2017)	Particle mass, flow rate, diameter Distribution, spread coefficient, wind speed, gravity vector	Wall surface wear rate per unit time	Clean and sand-laden wind	Unspecified	Baelo Claudia site, Tarifa, Spain	Mathematical derivation, CFD simulation

simulation.

2.2. Boundary condition definition

2.2.1. Erosion model

After the mesh model finished, the next step was to determine the wind erosion calculation scheme. A systematic review indicated that wind erosion models have been extensively applied in soil science and earthen heritage conservation (Table 2). Although numerical formulations of the wind erosion modulus, implemented in Fluent to convert grid-point wind speed outputs into erosion rates, can capture spatial erosion variability, their applicability is constrained by oversimplified airflow and soil representations. For example, the small-watershed wind erosion formula (Dong, 1998), extended from multi-factor farmland erosion models (Woodruff and Siddoway, 1965), and the raw-soil wind erosion equation (Rong et al., 2004) were both developed under clean wind conditions. Direct application of these models to earthen heritage risks may underestimate erosion from sand-laden winds. Moreover, these models were designed for loose agricultural soils rather than cohesive rammed earth, which exhibits higher initiation thresholds. Single-factor regression models for earthen heritage (Qu et al., 1994) can characterize both sand-laden and clean wind erosion, but rely on the assumption of uniformly injected sand at wind tunnel inlets, which is inconsistent with the nonuniform particle distributions in natural wind-driven transport. Accordingly, these models were deemed unsuitable.

To more accurately represent the heterogeneous density distribution of sand grains in sand-carrying winds, this study adapted CFD-based erosion modeling for wind erosion assessment. The adopted framework couples Lagrangian particle-tracking formulations with fluid flow simulations to resolve particle trajectories. Transfer functions were constructed using particle impact dynamics parameters (impact velocity, angle, and kinetic energy rate) and wall surface characteristics to compute erosion rates (ANSYS Europe Ltd., 2025; Dosanjh and Humphrey, 1985). This approach enables spatiotemporal accumulation of erosion damage through discrete-phase trajectory tracking, captures the heterogeneity of particle density distributions in sand-laden winds, and represents the transition of wind–sand flow states (Pineda and Iranzo, 2017). In this study, the erosion rate (E_{Vi}, $unit:\ kg/m^2-s$) was defined as the mass loss per unit time and area on wall surfaces, calculated as the cumulative wear induced by discrete particle impacts.

Among candidate formulations, the Finnie model was selected owing to its validated accuracy and demonstrated applicability to limestone materials (ANSYS Europe Ltd., 2025; Pineda and Iranzo, 2017). The benchmark parameterization of Pineda and Iranzo (2017) for dense limestone ($\rho\_d \approx 2.09$ g cm^{-3}; porosity < 2 %) was adopted as the reference for calibrating the key Finnie constants K, V_0 and n in this study. The Western Xia Mausoleum rammed-earth samples showed an average dry density of 1.78 g cm^{-3} and porosity of 33.3 % (Wang et al., 2002), indicating weak cementation and high permeability. These properties make the material highly susceptible to moisture variation and particle detachment under intensified climatic stressors such as increased rainfall and stronger wind events. Compared with limestone, the earthen material's erosion threshold velocity is 35–48 % lower, confirming its higher climatic vulnerability.

Following the limestone reference of Pineda and Iranzo (2017), the Finnie parameters were recalibrated to reflect the mechanical behavior of rammed earth (Appendix B). The threshold velocity V_0 was reduced to 800–1000 m s^{-1} to account for its lower density and cohesion; the erosion constant K was increased to 1.8–2.2 times that of limestone to represent its higher porosity and weaker interparticle bonding; and the velocity exponent n (2.3–2.4) was selected within the lower–middle range of the brittle-material interval

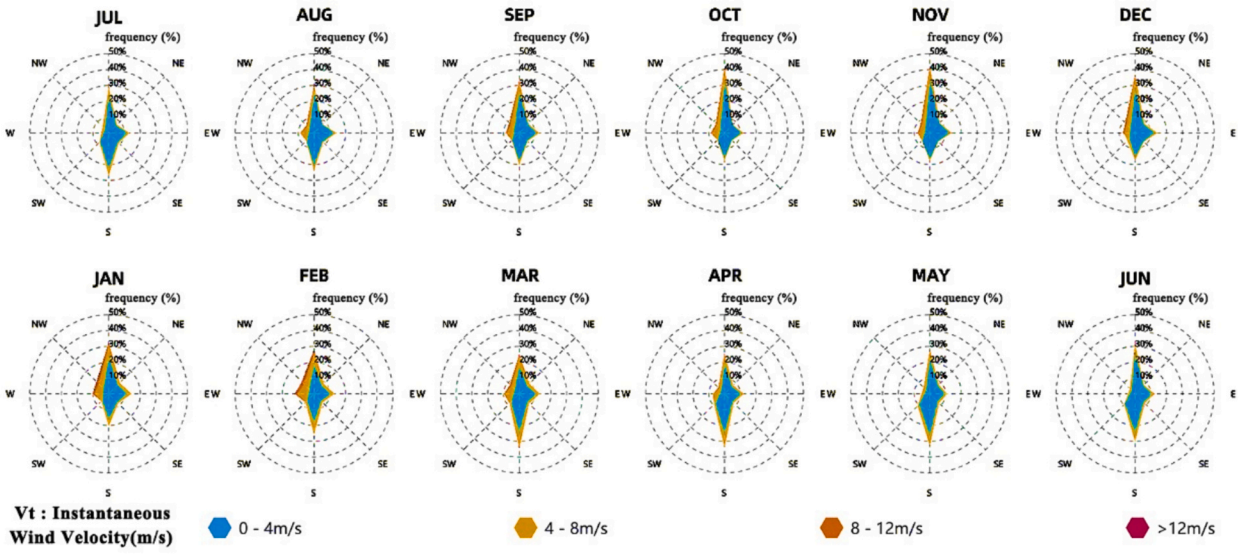

Fig. 4. Annual Wind Rose of Xixia Imperial Tombs *Synthesized from historical wind datasets (1956–2025) at multiple meteorological stations surrounding Yinchuan City*.

(2.3–2.5) recommended by ANSYS-CFX (ANSYS Europe Ltd., 2025), consistent with the granular structure and strong flow sensitivity of the material. These calibrated parameters ensured that the simulated erosion rates reproduced the observed surface disintegration of rammed-earth sections, aligning model performance with the in-situ geotechnical behavior.

The k–ε turbulence model was adopted for CFD simulation due to its established convergence stability and extensive validation in heritage conservation studies (Grau-Bové et al., 2019). This model is well-suited for resolving mesoscale velocity components (u, v, w) and turbulence parameters (k, ε). To account for feedback effects of high-concentration particle groups on the continuous phase under strong winds, the Interaction with Continuous Phase option was activated in the Fluent Discrete Phase Model.

2.2.2. Fluid phase

Wind erosion at the site was conceptualized as entrainment of near–surface particles by airflow, through suspension or leap, followed by particle–surface impacts leading to material loss. To represent fluid–particle interactions across a range of intensities, boundary conditions were defined for both the fluid (wind) and the solid (particles).

For the fluid phase, boundary conditions were derived from hourly wind records (1956–2025) from three meteorological stations around the Western Xia Mausoleums, totaling over 120,000 entries (at 0.1 m/s resolution). Datasets were obtained from the NOAA Global Meteorological Network and the China Environmental Weather Data Service Platform (Appendix C). Wind rose analysis indicated dominant north–south monsoonal winds (Fig. 4), with long-term monthly mean speeds of ~ 4 m/s and extreme instantaneous speeds up to 34 m/s, with high-wind events concentrated in autumn and winter.

Regarding the definition of wind speed, the initiation of surface particle movement by wind fluid has a critical threshold. Wind-tunnel experiments in northwestern China showed that particle-laden winds initiate erosion of earthen heritage only when surface wind speeds exceed 8 m/s (Yan et al., 2009). Under these conditions, erosion rates can exceed those under clean-wind conditions by > 130 times (Qu et al., 1994). This 8 m/s threshold is consistent with the "dust-raising wind" criterion (5.5–7.9 m/s) of the China administration (China Meteorological Administration, 2012) and was therefore adopted as the erosion initiation threshold in this study. Given its empirical support and regulatory consistency, the 8 m/s critical value was adopted as the erosion initiation threshold.

Analysis of historical wind data indicated that hourly wind speeds > 22 m/s occur at a probability of 7.5×10^{-5}, representing rare events with negligible effect on cumulative erosion estimates. Accordingly, thirty boundary cases were defined in this study: fifteen each for southerly and northerly winds spanning 8–22 m/s (Appendix D). Other air properties were set to default values, and a reference height of 10 m was used to maintain consistency with meteorological standards.

2.2.3. Solid phase

Field observations at the Xixia Imperial Tombs indicated that wind erosion primarily manifests as basal undercutting from impact and abrasion by sandy soil particles, combined with upper-wall erosion during sandstorm events (Lin et al., 2009). To replicate these mechanisms, an injection-surface approach was adopted, treating the off-site ground as a uniform particle emission zone. Particles were introduced with near-zero initial velocity to simulate natural deposition (Fig. 5), and particle flow rates were assigned as functions of external wind conditions. The assignment was based on a wind-tunnel dataset describing the relationships among soil type, moisture content, and erosion rate (Rong et al., 2004). The ground mass loss rate per unit area was defined as the injection surface flow rate, measured by an on-site wind tunnel device. Considering the sandy soil type and mean moisture content (3.83 %) in the Yinchuan region, the corresponding erosion loss-rate formula (Eq. (2)) was applied. Detailed particle flow rate assignments are provided in Appendix E.

Particle size distributions followed the widely applied Rosin–Rammler model (Alderliesten, 2013), characterized by the cumulative mass fraction Y_d and spread parameter N (Eqs. (3) and (4)). Based on the most detailed particle-size dataset available for rammed earth at the Xixia Imperial Tombs (Wang et al., 2002), parameters were calculated as $Y_d = 0.368$ and $N = 0.494$. Additional injection parameters are listed in Appendix E

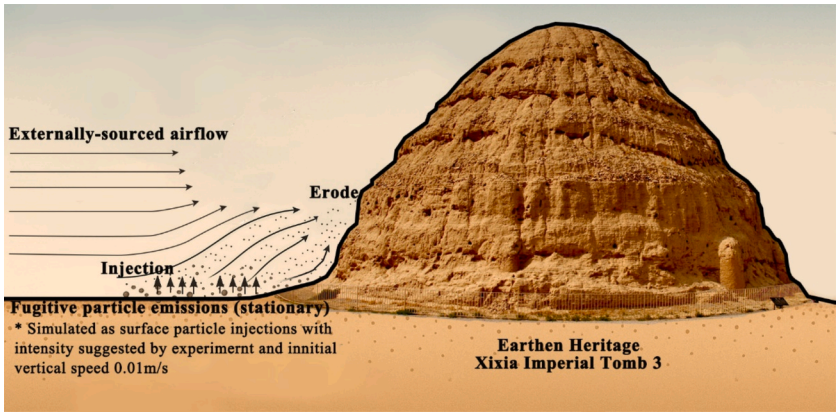

Fig. 5. Schematic representation of ground surface particle lifting.

$$FlowRate = \frac{0.0045e^{0.3328*V}}{5.5} * S_G/1000 \quad (2)$$

S_G: *CFD computational domain* (m^2)

$$\boldsymbol{Y_d = e^{-\left(\frac{d}{\bar{d}}\right)^N}} \quad (3)$$

$$\boldsymbol{N = \frac{ln(-lnY_d)}{ln\left(\frac{d}{\bar{d}}\right)}} \quad (4)$$

2.3. Multi-condition erosion simulation

2.3.1. Moisture resistance correction

After preparing the mesh model and fluid-particle parameters (Steps 2.1–2.3), simulations using the Finnie erosion model yielded the erosion rate intensity E_{Vi} for each unit grid cell under 30 wind conditions. Results for southerly and northerly winds were designated as $E_{Vi,S}$ and $E_{Vi,N}$. The wind erosion resistance of soil is significantly influenced by soil moisture content, which could be influence by the rain and water vapor in case site. Therefore, we corrected the primary erosion result to account for moisture-dependent resistance as:

$$E^*(Vi, \theta) = f_s(\theta_g) * f_e(\theta_s) * E_{Vi} \quad (5)$$

Where E_{Vi} is the baseline primary erosion result as erosion rate intensity ($kg/m^2 - s$) on a unit mesh cell of the heritage induced by south wind ($E_{Vi,S}$) or north wind ($E_{Vi,N}$) at specified levels of wind speed (Vi). θ_g is the gravimetric moisture content of the ground soil, and θ_s is those of the earthen structures. f_s is the stationary resistance coefficient calculated by the different fitting results from on-site wind tunnel experiment (Rong et al., 2004). Considering the limitation on the experiment result, predictions were divided into rain period ($\theta > 4.9\%$) and dry period ($\theta < 4.9\%$). The injection rate of stationary was calculated and assumed to be positively related to the erosion:

$$f_s(\theta_g) = I(\theta_g)/I(\theta_0 = 3.5) \quad (6)$$

f_e is the erosion resistance coefficient calculated by empirical equation suggested in the experiment (Govers et al., 1990; Moragoda et al., 2022) with similar earth properties (Wang et al., 2002):

$$Ln(E^*/E_d) = \sigma\theta^2 - b\theta \quad (7)$$

Here E^* is the erosion rate ($kg/m^2 - s$) at a given moisture content θ and E_d is the dry soil erosion rate. The original erosion rate is regarded as the maximum erosion value at the driest condition ($\theta_0 = 3.5\%$), with wetter conditions reducing erosion accordingly. The experiment S3 (Govers et al., 1990) is the closest soil to the site, with $\sigma = 0.1948$ and $b = 9.4951$ ($R^2 = 0.962$):

$$\boldsymbol{f_e(\theta_s) = exp\{\sigma(\theta_0^2 - \theta_s^2) - b(\theta_0 - \theta_s)\}} \quad (8)$$

Although the moisture content will vary in the future, the fluctuations of content are relatively small and have been ignored in the calculation. The monthly soil moisture content (3.5 % in January to 5.3 % in August) (Xiangjin Meng et al., 2021) was used in the above corrections.

2.3.2. Erosion intensity calculation

To further quantify the duration of wind erosion events and the annual distribution of wind directions, the daily average wind speed (V_D) and hourly wind speeds (Vi) for each period within the same day were statistically analyzed. The percentage of hours per day exceeding the erosion-initiation threshold of 8 m/s was defined as $P_{Vi,D}$, and corresponding charts were generated. Monthly probabilities of southerly and northerly winds, $P_{S,D}$ and $P_{N,D}$. Wind directions within (90°, 270°] were classified as southerly (S); all others were categorized as northerly (N).

The simulation outputs included boundary wind condition–erosion mass flow rate relationships, which revealed erosion severity across wind speed gradients and identified high-erosion conditions as key warning indicators. Comparative analysis of erosion under different prevailing wind directions informed the design of targeted windbreak strategies. Additionally, based on the E_{Vi} results, the annual erosion spatial intensity Q_y (kg/m^2) for each unit mesh cell was calculated by coupling daily operational conditions using Eq. (9). This framework enabled the generation of typical annual Q_y distribution maps, visually highlighting erosion hotspot areas across the heritage site.

$$\boldsymbol{Q_y = 24 \cdot 3600 \cdot \sum_{D\in(1,365)^*} \left(P_{S,D} \cdot \sum_{Vi\in(8,22)} P_{Vi,D} \cdot E_{Vi,S} + P_{N,D} \cdot \sum_{Vi\in(8,22)} P_{Vi,D} \cdot E_{Vi,N} \right)} \quad (9)$$

Q_y: Annual erosion spatial intensity for a unit mesh cell in year y (kg/m^2).

D: The Dth day of the year (365 or 366), dimensionless.
$P_{Vi,D}$: The percentage of hours per day during which the wind speed exceeded the erosion-initiation threshold (8 m/s).
$P_{S,D}$, $P_{N,D}$: probability (%) of south wind (S) and north wind (N) occurring on the Dth day, statistically derived from wind rose data.
y: Year (2025–2100), dimensionless.

2.4. Future erosion projection

Following the acquisition of E_{Vi}, future near-surface wind conditions were projected at high temporal resolution using the CMIP6 downscaled gridded dataset for China (1979–2100) released by the National Tibetan Plateau Data Center (Zhou et al., 2023). Compared to earlier models, CMIP6 integrates the latest SSP–RCP scenarios, combining emission concentrations with socioeconomic pathways to objectively represent future climate, making it IPCC-recommended and widely used in climate-impact simulations.

This dataset was originally built by referencing the China Meteorological Forcing Dataset (CMFD) and integrating six GCMs (CanESM5, FGOALS-g3, GFDL-CM4, IPSL-CM6A-LR, MPI-ESM1-2-HR, MRI-ESM2-0), with 0.25° spatial resolution bias correction against CMFD. To address wind projection uncertainties, this study expanded GCMs selection to 12 independent models, based on two criteria: availability of daily mean near-surface wind data for SSP2-4.5/SSP5-8.5, and model independence (one per research institute to avoid correlated biases). Raw 12 GCM outputs (1979–2100 daily mean wind sequences) were retained to preserve short-term variability. All data were cropped to the study area and resampled to a uniform $1 \times 1°$ grid using bilinear interpolation for inter-model comparability.

Given the CMIP6 wind data's daily resolution (insufficient for hourly erosion-threshold exceedance assessment), this study aligned daily-mean wind speeds to historical hourly data to generate hourly wind series through 2100. Specifically, a mapping relationship between future daily average wind speed (V_D) and hourly critical wind speed occurrence probability ($P_{Vi,D}$) was established in Python using merge functionality, enabling estimation for future daily exceedance durations. Future prevailing wind directions were assumed to follow stable historical values of $P_{S,D}$ and $P_{N,D}$, based on the premise of consistent local wind patterns by 2100.

Using the future hourly exceedance probabilities and E_{Vi} results from Section 2.3, the annual erosion spatial intensity (Q_y) for any year was calculated via Eq. (9). Spatial integration over the grid domain (Eq. (10)) yielded the total annual erosion mass (M_y), and cumulative erosion mass up to year y ($M_{cum(y)}$) was further derived using Eq. (11). This methodology combined historical and future meteorological data with CFD-based simulations to achieve spatiotemporal quantification of wind erosion risk on a centennial scale.

Key outputs included annual M_y tables under SSP2-4.5 and SSP5-8.5 scenarios through 2100, enabling identification of high-erosion years for conservation planning. Cumulative erosion density maps from spatial integration of annual M_y, quantifying long-term climate impacts. Cumulative erosion volume loss rate (cumulative eroded mass divided by average rammed-earth density) and maximum erosion depth, providing site degradation indicators and supporting prioritization of protective interventions.

$$\boldsymbol{M_y} = \sum \boldsymbol{Q_y}^{*}\boldsymbol{A_n} \tag{10}$$

M_y: *Total annual erosion mass in year y, kg.*
A_n: *the area of the simulated unitmeshcelln*

$$\boldsymbol{M_{cum(y)}} = \sum\nolimits_{\boldsymbol{y}\in(2025,2100)} \boldsymbol{M_y} \tag{11}$$

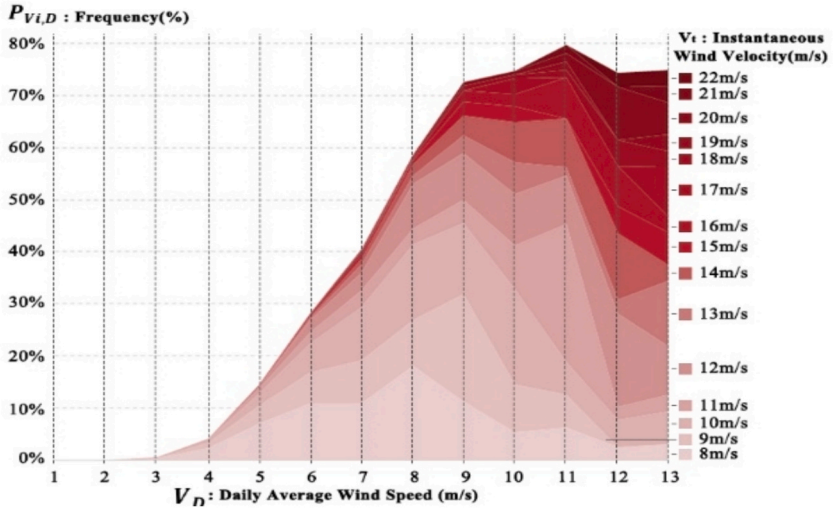

Fig. 6. Relationship between daily average wind speed ($\boldsymbol{V_D}$) and daily percentage of time during which hourly wind speed exceeded the critical threshold ($\boldsymbol{P_{Vi,D}}$) at Xixia Imperial No. 3 tomb (historical period).

Subsequent analysis employed the multi-model ensemble (ENS) mean of daily near-surface winds from 12 GCMs. For each GCM, daily mean wind speeds were aggregated into annual indicators (mean speed and frequency of strong winds > 8 m/s) to mitigate daily-scale variability before being input into the wind erosion model for 25-, 50-, and 75-year projections by component. The ENS mean for each erosion metric was calculated as the arithmetic average across all 12 GCMs to minimize individual model bias. To quantify CMIP6 wind uncertainty, standard deviation (std) values were derived from inter-model variability: for each calendar day, the 12 models' daily wind speeds defined a distribution whose std was aggregated into annual metrics. The resulting annual wind std was propagated to compute the std of each erosion metric (e.g., cumulative mass), producing ± 1 std bounds around the ENS mean. This method explicitly links erosion uncertainty to inherent CMIP6 wind variability.

3. Result

3.1. Hourly exceedance frequency of historical critical wind speeds

Fig. 6 shows the mapping results between the historical daily average wind speed (V_D) and the daily percentage of time during which hourly wind speed exceeded the erosion-initiation threshold ($P_{Vi,D}$). For instance, when $V_D = 12$ m/s (defined within the interval [12.5, 13.5] m/s), the percentage of hours with wind speeds above 22 m/s reached ~ 75 %, corresponding to ~ 18 h per day. This (V_D–$P_{Vi,D}$) mapping function provides a probabilistic link between mean daily conditions and extreme hourly exceedance frequencies. It was subsequently applied to future CMIP6 daily wind speed projections, enabling estimation of the temporal duration of threshold exceedance under different climate scenarios. By integrating this relationship with erosion rate intensities (E_{Vi}) and directional probabilities ($P_{S,D}$, $P_{N,D}$), the framework facilitated the calculation of annual erosion spatial intensity (Q_y) for each unit mesh cell across the projection period (2025–2100).

3.2. Spatial variability of Present-Day wind erosion

3.2.1. Boundary wind conditions and erosion rate

Fig. 7 illustrates the spatial distribution of erosion rate intensity under wind speeds of 8 m/s and 22 m/s. At 22 m/s, high-risk erosion zones expanded substantially relative to 8 m/s. Under southerly winds, the eastern base of the mausoleum pagoda and the inner surface of the eastern wall exhibited markedly higher erosion intensities compared with northerly winds.

Fig. 8 quantifies erosion mass flow rates for six heritage components under graded wind speeds, derived from the spatial integration of erosion rate values across corresponding grid cells. The eastern and northern walls exhibited the highest erosion rates, whereas the sacrificial hall and mausoleum pagoda showed lower values, indicating a shielding effect of the four low walls on interior structures. A critical wind speed of ~ 14 m/s was identified as an acceleration turning point, beyond which erosion rates increased sharply. To statistically determine this threshold, erosion-rate curves were log-transformed to offset exponential growth patterns. Each measurement series was robust-scaled, and a representative log-linear curve was constructed using the pointwise median. The optimal breakpoint between the initial plateau and subsequent log-linear increase was located using the L-method, which minimizes the combined residual sum of squares from two consecutive regressions. The boundary wind velocity (V_i) at this breakpoint was reported as the onset of accelerated erosion. This threshold provides a key reference for micro-meteorological monitoring and early warning systems at the Xixia Imperial Tombs.

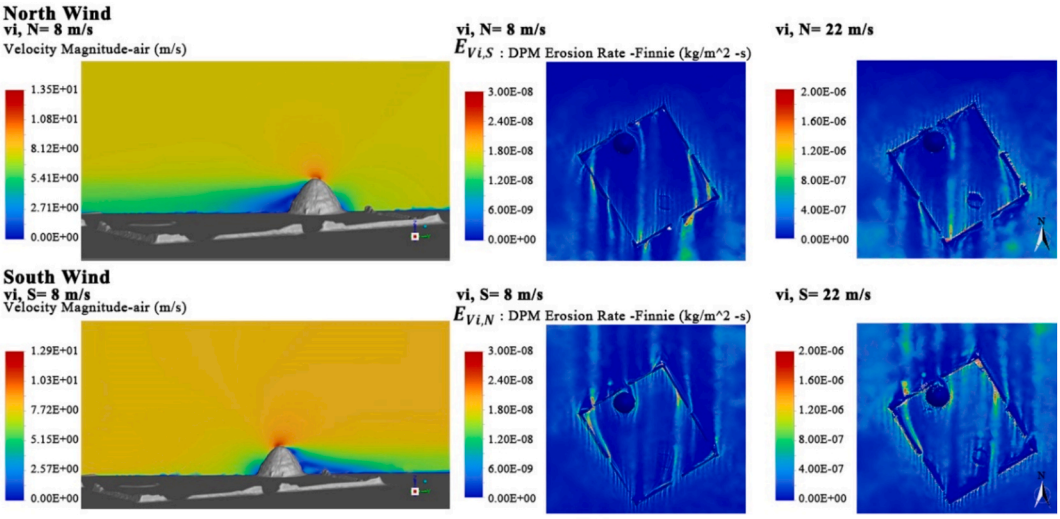

Fig. 7. Spatial distribution of erosion rate intensity ($E_{Vi,S}/E_{Vi,N}$) on unit mesh cells of the heritage at the Xixia Imperial No. 3 tomb under 8 m/s and 22 m/s wind conditions.

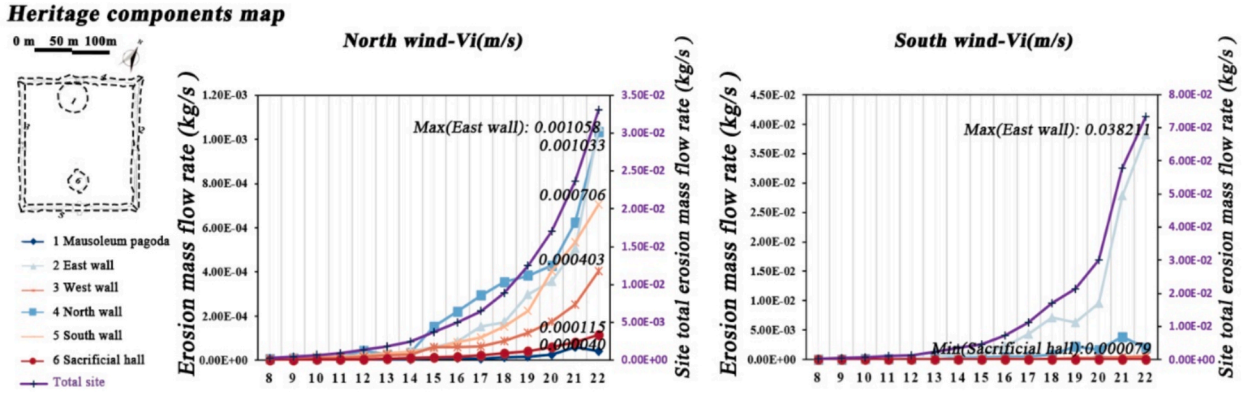

Fig. 8. Erosion mass flow rate of six heritage components and site total under northerly and southerly wind scenarios.

Also, Fig. 8 shows significant differences in erosion observed under different prevailing wind directions. Under northerly winds, erosion among the six components varied minimally. In contrast, the maximum erosion mass flow rate under southerly winds (0.03821 kg/s) was approximately 36 times greater than that under northerly winds (0.001058 kg/s), highlighting the need to prioritize reinforcement of southern-facing structures when conservation resources are limited.

Fig. 8 further shows that the total erosion mass flow rate in the computational domain followed a positive exponential relationship with boundary wind speed, consistent with wind tunnel results for rammed earth in northwestern Chinese heritage sites (Qu et al., 1994). Under unit-time conditions, erosion mass under southerly winds reached up to 2.22 times that under northerly winds, confirming the strong directional dependence of erosion processes. Additionally, erosion mass flow rate increased rapidly at wind speeds exceeding 10 m/s, indicating that this value represents the effective threshold for large-scale particle transport across the entire site.

3.2.2. *Spatial distribution of annual erosion intensity in a typical year*

Fig. 9 reveals the annual erosion spatial intensity (Q_y) for a typical year (2023–2024), calculated using Eq. (9). Results indicated that the inner surface of the eastern section of the northern gate–northern wall and the inner surface of the eastern section of the southern wall were the two highest-risk areas at the annual scale. The former resulted from the Coandă effect, whereby sand-laden southerly airflow was deflected by the hemispherical mausoleum pagoda, generating a circular airflow that substantially increased erosion density. The latter corresponded to the Venturi effect induced by the narrow gate opening in the eastern wall, which accelerated wind and particle impact.

3.3. *Future wind erosion projections under CMIP6 climate scenarios*

3.3.1. *Site-Wide erosion trends and scenario Comparison*

Fig. 10 shows the projected annual erosion mass and cumulative M_y of the main body of Xixia Imperial No. 3 tomb (2025–2100) under SSP2-4.5 and SSP5-8.5 scenarios in CMIP6 (calculated using Eqs. (9) and (10)). The kurtosis values indicated a sharper and more extreme annual distribution in SSP2-4.5, where "high-wind years" may occur more frequently. The coefficients of variation of RMSE were nearly identical, suggesting comparable relative interannual variability. The ranges of ± 1 and ± 2 standard deviations (std) were

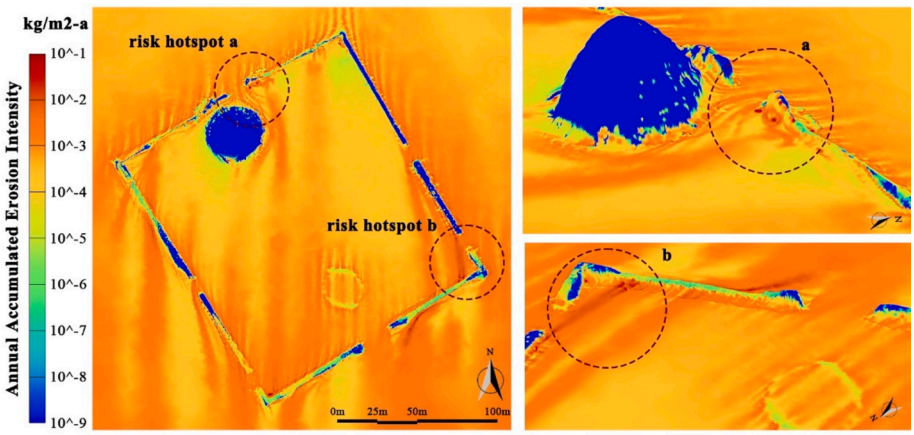

Fig. 9. Spatial distribution of annual erosion spatial intensity (Q_y) at the Xixia Imperial No. 3 tomb for a typical year (2023–2024).

also comparable, suggesting closely matched absolute interannual fluctuations and projection uncertainties. By 2100, cumulative erosion reached 67.0 × 10^3 kg (+1 std 192.3, +2 std 317.6 × 10^3 kg) under SSP2-4.5. The medium-forcing pathway (SSP2-4.5) yielded higher mean erosion and stronger interannual extremes, whereas SSP5-8.5 showed slightly lower totals but remained sensitive to extreme erosion events.

Table 3 quantifies the differences in cumulative erosion mass and volume under the two climate scenarios, calculated using Eqs. (9)-(11). By 2100, the SSP2-4.5 scenario yielded a 7.3 % greater mean erosion mass and a 0.008 percentage points higher volume-based erosion rate than SSP5-8.5. Contrary to initial assumptions, the high forcing scenario resulted in less severe cumulative erosion than the moderate scenario at this open-air heritage site. Both scenarios demonstrated substantial uncertainty intervals (±1 std), indicating a strong likelihood of extreme erosion outcomes substantially deviating from mean projections. This uncertainty underscored how reliance on mean estimates would significantly underestimate potential risks. The findings emphasized the critical importance of integrating uncertainty analysis into heritage conservation planning, necessitating the development of adaptive protection strategies to address the highly variable erosion risks under future climate conditions.

3.3.2. *Component-Specific erosion characteristics*

Fig. 11 further illustrates the spatial distribution of cumulative erosion density for the three heritage components by 2050, 2075, and 2100. Overall, extensive scouring was observed at the bases of multiple structures, including the mausoleum tower, displaying a persistent trend of vertical expansion over time. Specifically, a honeycomb-like erosion pattern developed on the southern and northeastern faces of the mausoleum pagoda. The inner and outer surfaces of the eastern wall exhibited comparable erosion severity, whereas the outer surface of the northern wall sustained greater damage than the inner surface.

To refine wind erosion assessment across heritage components, Appendix F presented predicted cumulative volume loss rates and maximum erosion depths under two climate scenarios using the ensemble mean model (ENS). Component-level data validated site-wide trends, with erosion metrics under SSP5-8.5 slightly lower than under SSP2-4.5; for example, the East wall's erosion mass was ~ 7.8 % lower. Distinct spatial heterogeneity in erosion intensity was observed. The East wall was the most vulnerable, with an eroded volume rate of 0.519 %, ~129 times that of the least vulnerable Mausoleum pagoda (0.004 %). The east and north walls showed high vulnerability, while the Mausoleum pagoda and the Sacrificial hall remained stable.

Maximum erosion depth was calculated as the average depth of the top 5 % most eroded grid cells after outlier removal. Prediction results indicated the eastern wall as the component with the most severe potential risk, with a projected mean depth of 239.8 mm by 2100 (average 3.2 mm/year). High-risk areas were primarily located at the base of the inner surface of the northeastern wall, providing critical information for targeted conservation strategies. The sacrificial hall exhibited the smallest cumulative erosion depth, followed by the mausoleum pagoda, indicating relatively uniform erosion rate distributions across their surfaces.

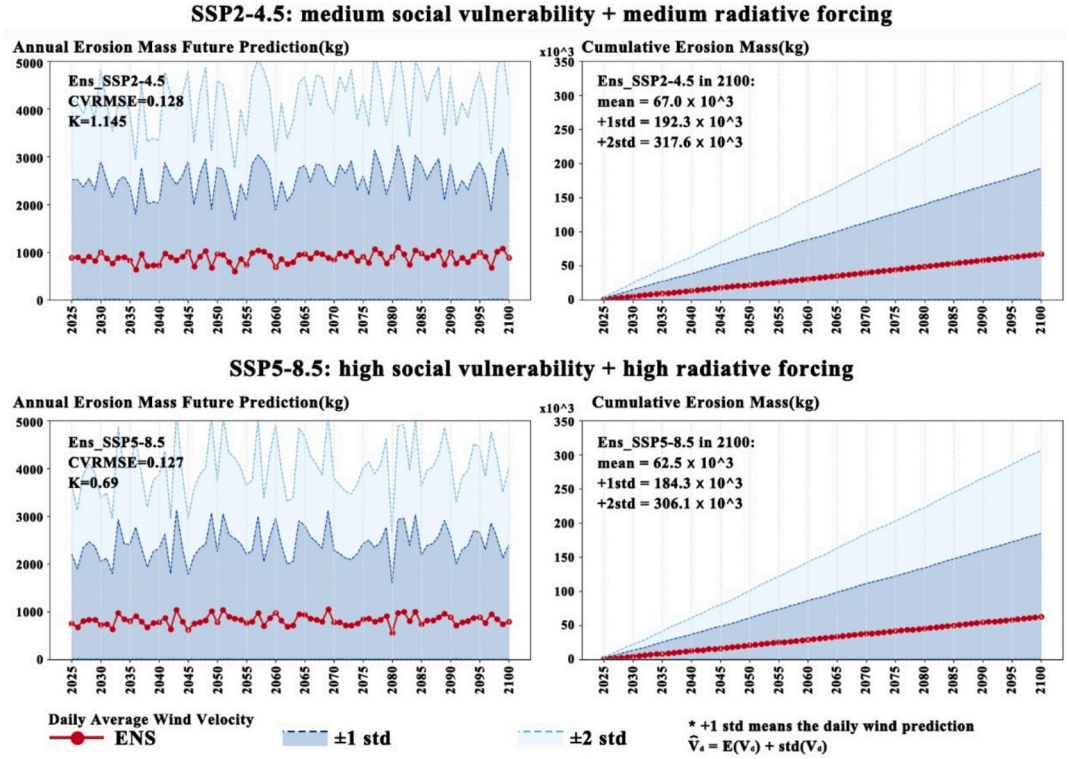

Fig. 10. Projected annual erosion mass (M_y) for Xixia Imperial No. 3 tomb under SSP2-4.5 and SSP5-8.5 climate scenarios (2025–2100).

Table 3
Total erosion mass and volume of No. 3 tomb heritage entities under SSP2-4.5 and SSP5-8.5 scenarios (2025–2100).

Climate Scenarios		Erode mass (kg)			Erode volume (m^3)			Erode (%)		
		25 yr (till 2050)	50 yr	75 yr	25 yr	50 yr	75 yr	25 yr	50 yr	75 yr
SSP2-4.5	−1std	247.83	515.03	764.44	0.14	0.29	0.43	0.000	0.001	0.001
	mean	22222.41	44261.99	67069.93	12.48	24.86	37.67	0.038	0.076	0.115
	+1std	63499.11	126616.70	192365.59	35.67	71.12	108.05	0.109	0.216	0.329
SSP5-8.5	−1std	227.92	446.54	636.34	0.13	0.25	0.36	0.000	0.001	0.001
	mean	20644.09	41558.69	62519.02	11.60	23.34	35.12	0.035	0.071	0.107
	+1std	60463.97	122055.63	184313.21	33.96	68.56	103.53	0.103	0.209	0.315

Note: Initial total volume of Xixia Imperial No. 3 tomb in 2025. All erosion values are relative to this 2025 baseline volume ($V^* = 32851.6\ m^3$).

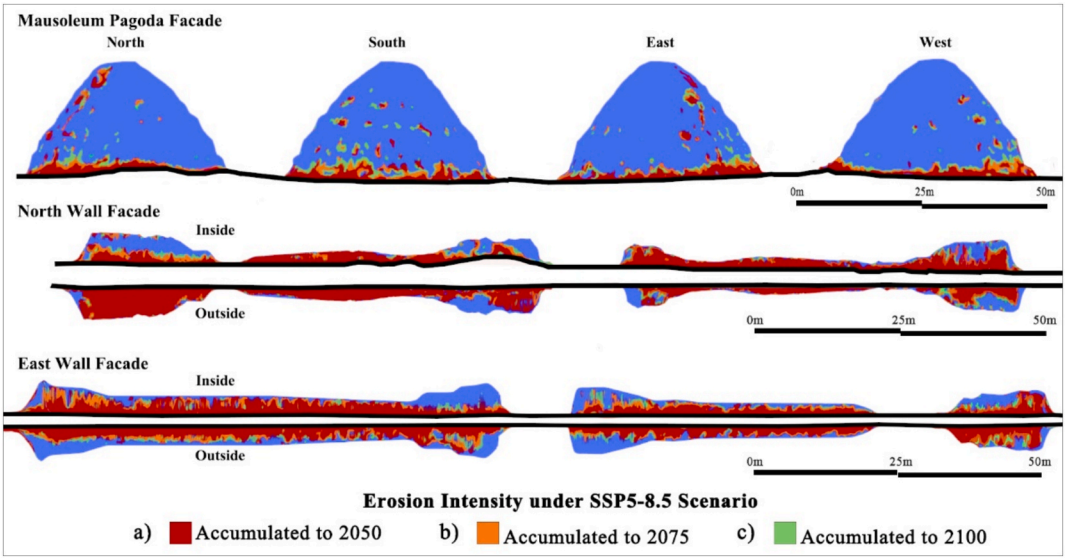

Fig. 11. Spatiotemporal evolution of cumulative erosion intensity (Q_y) at the Xixia Imperial No. 3 tomb under the SSP5-8.5 scenario (2025–2100). *Red zones indicate areas where the erosion density exceeded the benchmark threshold of 0.01 kg/m^2 by 2050 (relative to the 2025 baseline volume). Blue zones represent areas that remained below this threshold. Orange and green zones depict areas newly surpassing the threshold by 2075 and 2100. *. (For interpretation of the references to colour in this figure legend, the reader is referred to the web version of this article.)

Based on the simulated spatial distribution of erosion depth, early-warning and stabilization measures were recommended to be considered preferentially for the northeastern and southeastern wall bases. Rather than definitive intervention sequencing, such prioritization could support more efficient resource allocation in alignment with preventive conservation principles.

3.4. Management implications and climate mitigation assessment

The framework supports research and provides a quantitative tool for heritage conservation practice. By incorporating windbreak indicators such as the wind reduction coefficient (Ux/U0), the integrated simulation method translates protective measures into cumulative erosion mass reduction ratios, offering an intuitive quantitative assessment of mitigation benefits. Among natural solutions,

Table 4
Efficacy of windbreak strategies on cumulative erosion mass for No. 3 tomb under the SSP5-8.5 scenario (2025–2100).

Strategy	Porosity (Po, %)	Distance (Di)	Ux/U0	Erode Mass (kg)	Erode Volume (m^3)	Erode Volume Loss (%)
Non-intervention	–-	–-	1.0	67069.93	37.67	0.116 %
Strategy A	27	28H	0.9	34724.48	19.50	0.060 %
Strategy B	50	15.8H	0.8	17091.63	9.60	0.029 %
Strategy C	50	12.5H	0.7	7235.96	4.06	0.012 %
Strategy D	44–55	10H	0.6	2439.86	1.37	0.004 %
Strategy E	44–50	8.8H	0.5	919.59	0.52	0.002 %

*Note: H represents the average height of shelterbelt trees. For the Xixia Imperial Tombs, located in a desert-steppe zone, the natural vegetation height ranges from 0.3 to 1.2 m (Su et al., 2018); thus, H = 0.75 m was used as the average.

shelterbelts are typical: existing studies indicate that their protective effects can be quantified through relationships between Ux/U0 and parameters including porosity, width, relative distance, and vegetation morphology (Hao Wang et al., 2001). Using these relationships, this study evaluated potential erosion reduction for Tomb No. 3 under the worst-case SSP5-8.5 scenario (Table 4). Results indicate that, relative to the non-intervention baseline in 2025 (Ux/U0 = 1), optimal protection is achieved with shelterbelt porosity of 40–50 % or a distance of 8.8 H from the site: by 2100, cumulative volume loss is reduced by ~ 0.14 % compared to the baseline. Practical vegetation planning must still comply with safety distances and landscape management principles.

Di denotes the downwind distance from the heritage site to the shelterbelt.

Po refers to porosity, defined as the degree of ventilation openness within the shelterbelt structure, representing the proportion of wind that can pass through.

Ux/U0 is the wind speed reduction coefficient, where U0 is the undisturbed upstream wind speed and Ux is the average downwind wind speed after shelterbelt intervention. A lower Ux/U0 value indicates greater wind reduction efficacy. Due to the erosion-initiation threshold of 8 m/s for the rammed earth, scenarios with Ux/U0 $<$ 0.4 (requiring hourly wind speeds $\geq$ 20 m/s) were deemed statistically unnecessary for analysis. *.

4. Discussion

This study presents a unique cross-scale methodological integration that combines centimeter-resolution LiDAR, high-resolution CFD simulations under 30 wind conditions, and multi-scenario CMIP6 climate projections to quantify wind erosion risk for earthen heritage under climate change. Previous studies with simplified geometries and limited wind conditions (Chen et al., 2020; Richards et al., 2019; Yan et al., 2009) established baseline processes (Table 5). Unlike these single-condition or steady-state approaches, the present framework operates adaptively under multiple climate pathways (SSP2–4.5 and SSP5–8.5), enabling dynamic assessment of erosion responses across contrasting emission trajectories.

Spatially, the multi-condition design with 30 boundary wind cases produced site-wide erosion maps and captured nonlinear responses across wind-speed gradients. A critical threshold of ~ 14 m/s at the Xixia Imperial Tombs marked a sharp rise in erosion, complementing earlier initiation estimates of ~ 8 m/s (Yan et al., 2009) and illustrating the shift from onset to acceleration. Similar behavior has been observed in wind tunnel tests on rammed earth at Jiayuguan Fortress, where erosion remained limited under low winds but intensified rapidly at higher speeds (Chen et al., 2020). While specific to the study site, the 14 m/s threshold provides a practical benchmark for monitoring and management, enabling real-time alerts through on-site anemometers, preemptive protection using short-term forecasts, and seasonal planning during high-wind periods. It also supports cost-effective design by targeting reductions below the critical speed rather than full suppression.

Leveraging enhanced spatial resolution, this study incorporated mechanistic fluid–structure interactions driven by sediment-laden wind to improve fidelity in representing site-specific erosion processes. Previous studies assuming linear correlations between wind pressure and erosion often neglected particle impacts, mechanically aligning erosion with pressure fields (Shang, 2023). By separately modeling fluid flow and particle dynamics, this study simulated realistic wind-driven entrainment and impact processes, consistent with evidence that sand-laden wind dominates rammed-earth erosion, whereas unladen wind contributes minimally (Qu et al., 1994; Yan et al., 2009).

Temporally, our approach integrated historical hourly data with future daily projections to capture interannual variability and long-term trends. This contrasts with previous studies relying primarily on remote sensing for current-state assessments (Chen et al., 2023; Q. Guo et al., 2025) or linear extrapolations for future projections (Pineda and Iranzo, 2017), which may not fully account for non-stationary climate dynamics. We found that SSP2-4.5 exhibited higher interannual volatility and greater cumulative erosion by 2100, posing a dual threat of acute damage years and long-term degradation. In contrast, SSP5-8.5 showed more gradual increases. Both pathways demonstrated substantial uncertainty intervals, indicating a significant likelihood of extremes exceeding mean projections. Consequently, adaptation strategies require scenario-specific approaches, with SSP2–4.5 necessitating enhanced resilience to acute extremes and SSP5–8.5 emphasizing long-term durability. The pervasive uncertainty across scenarios underscores the need for robust, adaptive management plans.

Despite these advancements, this study has several limitations. Simulations indicated more severe erosion on the northern side of the mausoleum pagoda, consistent with visual surveys, but quantitative comparisons are still lacking. Model calibration is essential for improving reliability and transferability. However, systematic field monitoring remains unavailable, preventing rigorous validation. Future work will combine wind-tunnel experiments and digital image correlation (DIC) techniques to progressively achieve coupled validation between simulated and observed data.

Desiccation under high-temperature and low-moisture conditions was not explicitly modeled owing to current computational constraints and CFD solver limitations. While modern CFD solvers such as ANSYS Fluent offer advanced capabilities for fluid–solid and thermal interactions and particle transport, their publicly available standalone modules still lack stable, validated implementations for fully coupled thermo–hygro–mechanical (THM) processes, including crack initiation, crack propagation, shrink–swell deformation, and porosity evolution driven by temperature and moisture variations. Future work will incorporate rainfall–temperature–moisture interactions through multiphysics coupling, integrating crack-propagation and soil-moisture diffusion models validated by controlled wind–rain experiments to better represent desiccation-driven deterioration.

Moreover, the current analysis focused on averaged soil mechanical properties to represent the rammed-earth material. Detailed mineralogical and compositional heterogeneity, which may influence cohesion, permeability, and weathering resistance, was not examined. Future studies will include microstructural and compositional analyses to better capture intra-site variability and its effects on long-term degradation.

Table 5
Comparative Analysis of Wind Erosion Assessment Studies for Cultural Heritage.

Item 1: Comparison of Spatial Modeling and Geometric Precision

Study	Object Geometric Scale	Wind Condition Coverage	Number of Wind Speed Gradients	Number of Simulated Conditions	Key Spatial Outputs
(Yan et al., 2009)	Wind tunnel soil sample (25–49.6 cm^2)	Clean / Sand-carrying*Single direction	21 (0–20 m/s)	21	Wind erosion modulus ($kg{\cdot}m^{-2}{\cdot}h^{-1}$)
(Richards et al., 2019)	Single test wall	Clean / Sand-carrying / Rainfall*Single direction	3	3	Maximum erosion depth (mm) Erosion area percentage
(Chen et al., 2020)	Small soil block (7.07 cm^3)	Sand-carrying*Single direction	4	4	Wind erosion rate ($g{\cdot}min^{-1}$)
(Pineda & Iranzo, 2017)	Simplified site geometry	Sand-carrying*2 directions	3	6	Global erosion rate densityTotal erosion mass
(Shang, 2023)	Simplified site geometry	Clean wind*2 directions	2	4	Wind pressure/velocity distribution
This study	**Centimeter-scale LiDAR full-site geometry**	**Sand-carrying* 2 directions**	**15(8–22 m/s)**	**30**	**Full-site erosion rate density Volume loss rate Erosion depth**

Item 2: Comparison of Temporal Resolution and Future Scenario Methods

Study	Input Parameters	Future Scenarios	Output Temporal Resolution	Prediction Method
(Chen et al., 2023)	~7 years remote sensing	–-	Single cumulative distribution value	–-
(Q. Guo et al., 2025)	~4 years observed values	–-	4-year cumulative depth	–-
(Richards et al., 2020a)	–-	2 extreme scenarios	Single 100-year value	Superposition via cellular automata
(Pineda & Iranzo, 2017)	Typical year erosion mass	–-	Point values for typical year/50/100 years	Linear extrapolation
This study	**63 years of hourly wind data**	**CMIP6 (multiple SSPs)**	**Daily/Annual values (2025–2100)**	**Historical hourly × future daily downscaling**

Beyond physical simulations, future research could integrate data-driven and interpretable modeling approaches. Recent studies, such as water-erosion risk prediction for the Great Wall under CMIP6 scenarios (Tianlian Wang et al., 2025) and causal–explainable air-quality frameworks (Fu et al., 2025), demonstrated the value of combining predictive modeling with explainable analytics to identify key environmental drivers. Incorporating such methods could extend the present CFD–CMIP6 framework toward explainable erosion prediction and transparent attribution of risk factors under climate change.

Regarding applicability, the integrated predictive framework was developed and tested for the Xixia Imperial Tombs, and its broader transferability should be interpreted cautiously. Site-specific calibration parameters (such as soil cohesion, roughness, and terrain) strongly influence erosion dynamics. Consequently, direct application to other sites may require localized parameterization and validation. Computational cost and data availability also constrain scalability, especially for large or morphologically complex heritage landscapes. These considerations define the boundaries of generalization and highlight the need for multi-site validation in future research.

5. Conclusion

This study developed a coupled CFD–CMIP6 predictive framework to quantify long-term wind erosion risks for earthen heritage sites under climate change, achieving centimeter-scale spatial and centennial-scale temporal resolutions. Integrating high-resolution LiDAR models, site-scale CFD simulations, and multi-scenario CMIP6 climate projections, the framework offers a comprehensive approach that complements existing single-scale or static models. Coupling historical hourly meteorological records with future daily projections enables assessment of near-surface wind impacts under multiple climate pathways (SSP2–4.5 and SSP5–8.5), revealing how alternative emission trajectories may differentially shape earthen-heritage resilience.

The case study at the Xixia Imperial Tombs identified a nonlinear erosion threshold with spatially heterogeneous patterns, showing high-risk zones concentrated along the northeastern and southeastern wall bases. These spatial distributions guided optimized sensor placement and targeted stabilization strategies. Temporally, both climate scenarios projected gradual erosion increases from 2025, accompanied by substantial uncertainty intervals. The wide confidence bounds indicate a significant probability of erosion outcomes exceeding mean projections under both pathways. These findings emphasize the role of emission mitigation in altering degradation risks and inform adaptive conservation strategies, consistent with UNESCO's climate action for World Heritage (2021).

Compared with prior studies based on wind-tunnel experiments and static boundary conditions, this research integrates cross-spatiotemporal climate–fluid–solid interactions, enabling continuous long-term predictions. The framework reveals nonlinear threshold behaviors and spatially differentiated risk patterns under multiple climate scenarios, advancing both theoretical understanding of aeolian erosion mechanisms and practical heritage conservation applications. By incorporating protection indicators such as the wind-reduction coefficient (Ux/U0), it provides a quantitative tool for evaluating engineering effectiveness and supporting

cost–benefit optimization.

The framework's predictive accuracy relies on site-specific calibration at the Xixia Imperial Tombs, necessitating reparameterization for other locations. Key limitations involve scarce empirical validation, the CFD framework's inability to simulate thermo-hygro-mechanical processes such as desiccation cracking, and simplified soil representations that overlook mineralogical heterogeneity. Thus, the framework serves as a transferable methodological foundation for comparable earthen structures (such as earthen walls or fortresses) rather than a universally validated tool. Future work will incorporate wind–rain experiments, microstructural analysis, and interpretable modeling to strengthen generalizability under varied climatic and geomorphic conditions.

Declaration of generative AI and AI-assisted technologies in the writing process

In the writing process AI were used to improve the language of the manuscript.

CRediT authorship contribution statement

Qiong Wang: Writing – review & editing, Writing – original draft, Visualization, Validation, Supervision, Software, Resources, Project administration, Methodology, Investigation, Formal analysis, Data curation, Conceptualization. **Jun Xiao:** Writing – review & editing, Visualization, Validation, Supervision, Software, Resources, Methodology, Formal analysis, Data curation, Conceptualization. **Anrong Dang:** Writing – review & editing, Supervision, Resources, Investigation, Funding acquisition. **Xiuyun Xu:** Resources, Data curation. **Jingxiong Huang:** Supervision, Resources, Investigation. **Ruihua Zhang:** Supervision, Resources.

Declaration of competing interest

The authors declare that they have no known competing financial interests or personal relationships that could have appeared to influence the work reported in this paper.

Acknowledgements

This work was supported by National Key R&D Program of China [grant number No. 2024YFC3808500], and Scientific Research Project of the Forestry and Grassland Bureau of Ningxia Hui Autonomous Region (Grant No. 20242001585): Study on the Natural and Cultural Landscape Resources of Helan Mountain National Park in Ningxia (Sept. 2024–Aug. 2025). We are also grateful to Hao Zhou (School of Architecture, Tsinghua University) for his critical feedback on the initial draft.

Appendix A. Key parameters of the Xixia no. 3 tomb site

Parameters	Numerical value	Parameters	Numerical value
Height above sea level	1163 *m*	The case land area	1108.85 m^2
Deflection angle	30° north-west	The case total volume	32851.64 m^3
Thermo-climatic zone	temperate continental climate zone	Mausoleum Terrace average diameter top surface/ base surface	4 ~ 6m/37.5 *m*
The case surface area	1950.62 m^2	Mausoleum Terrace height(H)	21 *m*

Appendix B. Key parameters in finnie model

	Parameter	Definition
Main Geotechnical Properties (Wang et al., 2002)	Gravity	−9.81 m/s^2
	Turbulence Model	k-ε
	Materials −Solid Density	1780 kg/m^3(Wang et al., 2002)
	Materials- Particle Density	1500 kg/m^3(Yuanyuan Cheng and Paul C. Nathanail, 2009)
	DPM Tracking Parameters Max. number of steps	50,000
	Average Dry Density (ρ_d)	1.779 kg/m^3
	Average Specific Gravity (G_s)	2.68
	Average Void Ratio	0.509
	Average Porosity	33.29 %
	Average Disintegration Rate	19.696 g/min
Recommended Finnie Model Parameters	Reference Velocity (V_0)	800–1000 m/s
	Velocity Exponent (n)	2.3–2.4
	Erosion Constant (K)	1.8–2.2 times that of limestone (Pineda and Iranzo, 2017)

(*continued on next page*)

(*continued*)

	Parameter	Definition
Particle Injection	Diameter Distribution	Rosin- rammler (Alderliesten, 2013)
	Initial velocity	0.1 m/s
	Min. Diameter	7.5e-5 m (Wang et al., 2002)
	Max. Diameter	0.02 m (Wang et al., 2002)
	Mean Diameter	0.000231 m (Wang et al., 2002)
	Spread Parameter (N)	0.494
	Number of diameter	6
Boundary	Roughness Length (Z_0) for Sandy Soil	0.0010–0.0011 m (Joanna Rotnicka and Maciej Dłużewski, 2022)
	Wall-Sand grain roughness constant (C_S)	0.5(Bert Blocken et al., 2007)
	Wall-Sand grain roughness height (Ks)	0.021 m ($Ks = 9.793*z_0/C_S$) (Bert Blocken et al., 2007)

Appendix C. Historical wind environment dataset in the Xixia area

Station	Name	LAT, LON	Year	Resolution	Source
53,519,099,999	Shizuishan Dawukou, CH	39.05,106.4	1962–1997	3 ~ 6Hours/time, wind speed, 16 direction angle	Noaa, USA (Menne et al., 2012)
	Shizuishan, Huinong, CH	39.238537,106.781565	2023–2025.3.11	1 Hour/time, wind speed, 16 direction angle	Environmental Weather Data Service Platform, CH (Environmental meteorological data service platform, 2024)
53,614,099,999	Yinchuan, CH	38.4833333,106.2166667	1956–2023	3 ~ 6Hours/time, wind speed, 16 direction angle	Noaa, USA (Menne et al., 2012)

Appendix D. Simulated boundary conditions for external wind environment (8–22 m/s, Northerly/Southerly Winds)

N wind code	External wind speed	Injection flow rate (kg/s)	S wind code	External wind speed	Injection flow rate (kg/s)
N-1	8	1.710427	S-1	8	1.710427
N-2	9	2.38582	S-2	9	2.38582
N-3	10	3.327905	S-3	10	3.327905
N-4	11	4.641989	S-4	11	4.641989
N-5	12	6.474964	S-5	12	6.474964
N-6	13	9.031722	S-6	13	9.031722
N-7	14	12.59806	S-7	14	12.59806
N-8	15	17.57264	S-8	15	17.57264
N-9	16	24.51152	S-9	16	24.51152
N-10	17	34.19034	S-10	17	34.19034
N-11	18	47.69102	S-11	18	47.69102
N-12	19	66.52269	S-12	19	66.52269
N-13	20	92.79039	S-13	20	92.79039
N-14	21	129.4304	S-14	21	129.4304
N-15	22	180.5383	S-15	22	180.5383

Appendix E. Particle parameter settings

.

Table A
Ground Particle Size Distribution and Mass Fraction Percentage (*Yd*) at the Xixia Imperial Tombs.

d: Particle Size Range (μm)	Yd				
	Sample 1	Sample 2	Sample 3	Sample 4	Average Value
20,000	0	0.069	0.02	0.033	0.0305
2000–20000	0.233	0.231	0.147	0.219	0.2075
500–2000	0.062	0.042	0.068	0.037	0.05225
250–500	0.027	0.028	0.047	0.082	0.046
75–250	0.272	0.292	0.303	0.295	0.2905
−75	0.406	0.339	0.414	0.334	0.37325

Table B
Diffusion Coefficient (*N*) for Gravel Particle Size Distribution.

Particle Size (μm)	Cumulative Mass Fraction (Yd)	Spread Coefficient (*N*)
20,000	0.0305	0.280097
2000	0.238	0.167376
500	0.29025	0.274971
250	0.33625	1.07089
75	0.62675	0.67728
Average $N = 0.494$		

Appendix F. . Cumulative wind erosion metrics of heritage components at the Xixia Imperial no. 3 tomb under SSP2-4.5 and SSP5-8.5 scenarios (Mass, volume, and maximum depth)

Component		Mausoleum pagoda	East wall	South wall	West wall	North wall	Sacrificial hall
Initial Volume (m^3) in 2025		18617.24	4145.98	2150.74	3107.21	4392.01	438.46
SSP2-4.5							
Erosion Mass (kg)	25 yr (till2050)	418.50	12622.99	2233.43	1275.76	5406.11	268.40
	50 yr	833.05	25226.83	4423.97	2529.71	10721.32	532.53
	75 yr	1258.52	38317.87	6674.80	3821.39	16199.74	805.50
Erosion Volume (m^3)	25 yr	0.24	7.09	1.25	0.72	3.04	0.15
	50 yr	0.47	14.17	2.49	1.42	6.02	0.30
	75 yr	0.71	21.53	3.75	2.15	9.10	0.45
Erode (%)	25 yr	0.001 %	0.171 %	0.058 %	0.023 %	0.069 %	0.034 %
	50 yr	0.003 %	0.342 %	0.116 %	0.046 %	0.137 %	0.068 %
	75 yr	0.004 %	0.519 %	0.174 %	0.069 %	0.207 %	0.103 %
Maximum Erosion Depth* (mm)	25 yr	2.42	79.91	6.66	4.22	43.10	1.78
	50 yr	4.80	157.71	13.15	8.33	85.03	3.52
	75 yr	7.26	238.96	19.86	12.58	128.35	5.32
SSP5-8.5							
Component		Mausoleum pagoda	East wall	South wall	West wall	North wall	Sacrificial hall
Erosion Mass (kg)	25 yr	392.53	11574.26	2122.09	1205.84	5099.37	252.68
	50 yr	787.77	23396.64	4242.44	2416.56	10213.08	507.37
	75 yr	1181.66	35322.21	6344.23	3620.45	15296.51	761.56
Erosion Volume (m^3)	25 yr	0.22	6.50	1.19	0.68	2.86	0.14
	50 yr	0.44	13.14	2.38	1.36	5.74	0.29
	75 yr	0.66	19.84	3.56	2.03	8.59	0.43
Erode (%)	25 yr	0.001 %	0.157 %	0.055 %	0.022 %	0.065 %	0.032 %
	50 yr	0.025 %	0.738 %	0.134 %	0.076 %	0.322 %	0.016 %
	75 yr	0.169 %	0.171 %	0.168 %	0.169 %	0.169 %	0.169 %
Maximum Erosion Depth* (mm)	25 yr	2.42	79.91	6.66	4.22	43.10	1.78
	50 yr	4.80	157.71	13.15	8.33	85.03	3.52
	75 yr	7.26	238.96	19.86	12.58	128.35	5.32

*Note: Erosion Volume and Percentage are calculated relative to the 2025 initial volume. Maximum erosion depth represents the average depth of the top 5 % most eroded grid cells. A uniform rammed earth density of 1,780 kg/m^3 was applied for all calculations. *.

Data availability

Data will be made available on request.

References

Alderliesten, M., 2013. Mean particle diameters. Part VII. The rosin-rammler size distribution: physical and mathematical properties and relationships to moment-ratio defined mean particle diameters. Part. Part. Syst. Charact. 30 (3), 244–257. https://doi.org/10.1002/ppsc.201200021.

ANSYS Europe Ltd., 2025. CFX-Solver Theory Guide (p. 271). ANSYS Europe Ltd., Canonsburg, PA, USA. https://ansyshelp.ansys.com/public/account/secured?returnurl=/Views/Secured/corp/v251/en/cfx_thry/i1308811.html?q=finnie%20model (accessed 1 January 2025).

Hussein, A.S., El-Shishiny, H., 2009. Influences of wind flow over heritage sites: a case study of the wind environment over the Giza Plateau in Egypt. Environ Model Softw. 24 (3), 389–410. https://doi.org/10.1016/j.envsoft.2008.08.002.

Blocken, B., et al., 2007. CFD simulation of the atmospheric boundary layer: wall function problems. Atmos. Environ. 41 (2), 238–252. https://doi.org/10.1016/j.atmosenv.2006.08.019.

Chen, W., Wu, H., Yuan, P., Guo, Z., Liu, P., 2023. Sediment accumulation process in the remains of Suoyang City based on time series InSAR technology. J. Lanzhou Univ. (Nat. Sci.) 59 (05), 655–663. https://doi.org/10.13885/j.issn.0455-2059.2023.05.011.

Chen, W., Wu, H., Zhang, S., Chen, H., Qi, Q., Wu, C., Guo, Z., Ren, K., Yan, H., 2025. Study on the characteristics of aeolian sand movement and accumulation at the east wall of Suoyang Ancient City based on CFD. Eur. Phys. J. Plus 140 (2), 112. https://doi.org/10.1140/epjp/s13360-025-06051-3.

Chen, W., Xia, Y., Du, Y., Chen, H., 2020. Effect of wind erosions on earthen sites under the different water contents. J. Lanzhou Univ. (Nat. Sci.) CNKI 56 (06), 793–798. https://doi.org/10.13885/j.issn.0455-2059.2020.06.011.

China Meteorological Administration, 2012. Wind scale of the People's Republic of China (National Standard GB/T 28591-2012). China Standards Press, Beijing. https://www.eia543.com/documents/01%e6%b0%94/%e9%a3%8e%e5%8a%9b%e7%ad%89%e7%ba%a7%ef%bc%88GB%20T%2028591-2012%ef%bc%89.pdf (accessed 10 January 2025).

David Gandreau, Leticia Delboy, 2012. World Heritage: Inventory of earthen architecture. 2012. United Nations Educational, Scientific and Cultural Organization (UNESCO). http://unesdoc.unesco.org/images/0021/002170/217020e.pdf (accessed 5 December 2024).

Dong, Z., 1998. Establishing statistic model of wind erosion on small watershed basis. Bull. Soil Water Conserv. 5, 56–63. https://doi.org/10.3969/j.issn.1000-288X.1998.05.013.

Environmental meteorological data service platform. 2024. Hourly observation data of China surface weather data [Yinchuan hourly station data 2023–2025]. Eia-data.com. http://eia-data.com/era5_download/ (accessed 20 September 2024).

Fu, Z., Yang, X., Ma, Y., Sun, Y., Wang, T., 2025. Integrating explainable AI and causal inference to unveil regional air quality drivers in China. J. Environ. Manag. 390, 126270. https://doi.org/10.1016/j.jenvman.2025.126270.

Govers, G., Everaert, W., Poesen, J., Rauws, G., De Ploey, J., Lautridou, J.P., 1990. A long flume study of the dynamic factors affecting the resistance of a loamy soil to concentrated flow erosion. Earth Surf. Process. Landforms 15 (4), 313–328. https://doi.org/10.1002/esp.3290150403.

Grau-Bové, J., Mazzei, L., Strlic, M., Cassar, M., 2019. Fluid simulations in heritage science. Heritage Sci. 7 (1), 16. https://doi.org/10.1186/s40494-019-0259-9.

Gregory, J.M., Wilson, G.R., Singh, U.B., Darwish, M.M., 2004. TEAM: Integrated, process-based wind-erosion model. Environ Model Softw. 19 (2), 205–215. https://doi.org/10.1016/S1364-8152(03)00124-5.

Guo, Q., Huang, J., Pei, Q., Zhang, B., Zhan, H., Zhang, H., Richards, J., Viles, H., 2025. Erosion model for wind-blown sand flow at earthen sites in arid environment, Northwest China. Int. J. Architect. Heritage 19 (1), 96–111. https://doi.org/10.1080/15583058.2023.2267506.

Guo, Z., Qi, Q., Zhang, S., Chen, W., Wu, C., Wu, H., 2023. Study on the characterization of differential weathering feature based on surface roughness theory and 3D laser scanning: a case study of the Suoyang Ancient City. J. Cult. Herit. 62, 449–459. https://doi.org/10.1016/j.culher.2023.06.020.

Guo, Z., Wu, C., Zhang, S., Chen, W., Qi, Q., Wu, H., 2024. Characterization on flaking of rammed earthen sites using SMO algorithm and surface topography analysis: a case study of Jiaohe Ruins. J. Comput. Cultural Heritage 17 (3), 1–20. https://doi.org/10.1145/3673763.

Wang, H., Takle, E.S., Shen, J., 2001. Shelterbelts and windbreaks: mathematical modeling and computer simulations of turbulent flows. Annu. Rev. Fluid Mech. 33, 549–586. https://doi.org/10.1146/annurev.fluid.33.1.549.

Institute of Architectural History (China Architecture Design & Research Group), Western Xia Mausoleum Administrative Office, Ningxia Institute of Cultural Relics and Archaeology, 2020. Conservation master plan for the Western Xia Mausoleum National Cultural Heritage Site (2019–2035) (640000/2024-00048). https://www.nx.gov.cn/zwgk/qzfwj/202401/t20240122_4423973.html (accessed 4 March 2025).

Jiang, Y., Luo, Y., Zhao, Z., Shi, Y., Xu, Y., Zhu, J., 2010. Projections of wind changes for 21st century in China by three regional climate models. Chin. Geogr. Sci. 20 (3), 226–235. https://doi.org/10.1007/s11769-010-0226-6.

Rotnicka, J., Dłużewski, M., 2022. Vertical profiles of aeolian mass flux above different sand surfaces and sand surfaces covered with pebbles. Catena 212, 106006. https://doi.org/10.1016/j.catena.2021.106006.

Lin, Q., Wang, X., Guo, Q., Yang, S., Zhang, Y., 2009. Preliminary analysis on the status quo of salt hazard of the Western Xia Imperial tomb in Yinchuan: based mainly on No. 3 and No. 6. Dunhuang Res. 6, 75–80. https://doi.org/10.3969/j.issn.1000-4106.2009.06.016.

Long, Y., Xu, C., Liu, F., Liu, Y., Yin, G., 2021. Evaluation and projection of wind speed in the arid region of northwest China based on CMIP6. Remote Sens. 13 (20), 4076. https://doi.org/10.3390/rs13204076.

Correia, M., 2016. Conservation in Earthen Heritage: Assessment and Significance of Failure, Criteria, Conservation Theory, and Strategies. Cambridge Scholars Publishing, Newcastle upon Tyne, UK.

Menne, M. J., Durre, I., Korzeniewski, B., McNeill, S., Thomas, K., Yin, X., Anthony, S., Ray, R., Vose, R. S., Gleason, B. E., Houston, T. G., 2012. Global Historical Climatology Network – Daily (GHCN-Daily), Version 3.32 [global daily station data 1929–2024] [dataset]. NOAA National Centers for Environmental Information. https://doi.org/10.7289/V5D21VHZ.

Moragoda, N., Kumar, M., Cohen, S., 2022. Representing the role of soil moisture on erosion resistance in sediment models: challenges and opportunities. Earth Sci. Rev. 229, 104032. https://doi.org/10.1016/j.earscirev.2022.104032.

Woodruff, N.P., Siddoway, F.H., 1965. A wind erosion equation. Soil Sci. Soc. Am. J. 29 (5), 602–608. https://doi.org/10.2136/sssaj1965.03615995002900050035x.

Orr, S.A., Richards, J., Fatorić, S., 2021. Climate change and cultural heritage: a systematic literature review (2016–2020). The Hist. Environ.: Policy Pract. 12 (3–4), 434–477. https://doi.org/10.1080/17567505.2021.1957264.

Pineda, P., Iranzo, A., 2017. Analysis of sand-loaded air flow erosion in heritage sites by computational fluid dynamics: method and damage prediction. J. Cult. Herit. 25, 75–86. https://doi.org/10.1016/j.culher.2016.12.005.

Qu, J., Zhang, W., Wang, Y., He, D., Dai, F., Wen, Z., Wang, J., 1994. A study on the mechanism andthe prevention of wind erosion of ancient adobe construction in Mogao grottoes. Geogr. Res. 04, 98–104. https://www.dlyj.ac.cn/CN/10.11821/yj1994040013.

Richards, J., Bailey, R., Mayaud, J., Viles, H., Guo, Q., Wang, X., 2020a. Deterioration risk of dryland earthen heritage sites facing future climatic uncertainty. Sci. Rep. 10 (1), 16419. https://doi.org/10.1038/s41598-020-73456-8.

Richards, J., Mayaud, J., Zhan, H., Wu, F., Bailey, R., Viles, H., 2020b. Modelling the risk of deterioration at earthen heritage sites in drylands. Earth Surf. Proc. Land. 45 (11), 2401–2416. https://doi.org/10.1002/esp.4887.

Richards, J., Viles, H., Guo, Q., 2020c. The importance of wind as a driver of earthen heritage deterioration in dryland environments. Geomorphol 369, 107363. https://doi.org/10.1016/j.geomorph.2020.107363.

Richards, J., Zhao, G., Zhang, H., Viles, H., 2019. A controlled field experiment to investigate the deterioration of earthen heritage by wind and rain. Herit. Sci. 7 (1), 51. https://doi.org/10.1186/s40494-019-0293-7.

Rong, J., Zhang, H., Mao, N., 2004. Study on the changing laws of wind-blown mass affected by wind speed. Agric. Res. Arid Areas. 2, 149–153. https://doi.org/10.3321/j.issn:1000-7601.2004.02.032.

Sesana, E., Gagnon, A.S., Ciantelli, C., Cassar, J., Hughes, J.J., 2021. Climate change impacts on cultural heritage: a literature review. WIREs Clim. Change 12 (4), e710.

Shang, L., 2023. Restoration of Xixia Tomb Tower No. 3 and analysis of the existing relic environment [Master's Thesis]. Ningxia University, Yinchuan, China. https://link.cnki.net/doi/10.27257/d.cnki.gnxhc.2023.000732 (accessed 2 September 2025).

Shao, M., Li, L., Wang, S., Wang, E., Li, Z., 2013. Deterioration mechanisms of building materials of Jiaohe ruins in China. J. Cult. Herit. 14 (1), 38–44. https://doi.org/10.1016/j.culher.2012.03.006.

Su, C., Ma, W., Zhang, X., Su, Y., Min, Y., Zhang, J.Y., Zhao, L.Q., Liang, C.Z., 2018. Species composition and structure characteristics of the major montane shrub communities in the west slope of Helan Mountains, Nei Mongol, China. Chin. J. Plant Ecol. 42 (10), 1050–1054. https://doi.org/10.17521/cjpe.2018.0111.

Dosanjh, S., Humphrey, J.A.C., 1985. The influence of turbulence on erosion by a particle-laden fluid jet. Wear 102 (4), 309–330. https://doi.org/10.1016/0043-1648(85)90175-9.

Sun, M., Chen, Y., Shen, Y., 2022. New progress and prospects in research on earthen site deterioration. Dunhuang Res. 192 (2), 136–148. https://doi.org/10.13584/j.cnki.issn1000-4106.2022.02.001.

Wang, T., Fu, Z., Zhang, S., Li, Z., 2025. Water erosion risk assessment and predictive modelling for cultural heritage under climate change: a case study of the Great Wall in the Yellow River Basin, China. J. Clean. Prod. 510, 145645. https://doi.org/10.1016/j.jclepro.2025.145645.

UNESCO, 2008. List of factors affecting the properties. UNESCO, Paris, France. https://whc.unesco.org /en/factors (accessed 25 March 2025).

UNESCO, 2013. Earthen architecture in today's world. United Nations Educational, Scientific and Cultural Organization (UNESCO), Paris, France. https://unesdoc.unesco.org/ark:/48223/pf0000225481 (accessed 13 May 2025).

UNESCO, 2021. Updated policy document on climate action for World Heritage. United Nations Educational, Scientific and Cultural Organization (UNESCO), Paris, France. https://unesdoc.unesco.org/ark:/48223/pf0000390439 (accessed 13 May 2025).

UNESCO World Heritage Centre, 2025. Xixia Imperial Tombs. UNESCO World Heritage Centre, Paris, France. https://whc.unesco.org/en/list/1736/ (accessed 13 May 2025).

Wang, X., Zhang, L., Li, Z., Wang, C., Li, W., 2002. The study of existing condition and consolidation project of No. 3 Tomb of the Western Xia Mausoleums. Dunhuang Res. 4. https://doi.org/10.3969/j.issn.1000-4106.2002.04.011, 64–72+112–116.

Chen, W., Dong, Z.B., Li, Z.S., Yang, Z.T., 1996. Wind tunnel test of the influence of moisture on the erodibility of loessial sandy loam soils by wind. J. Arid Environ. 34 (4), 391–402. https://doi.org/10.1006/jare.1996.0119.

World Heritage Centre, 2021a. Climate change World Heritage n°100. UNESCO, Paris, France. https://whc.unesco.org/en/review/100.

World Heritage Centre, 2021b. World Heritage Earthen Architecture Programme (WHEAP). UNESCO, Paris, France. https://whc.unesco.org/en/earthen-architecture.

Meng, X.J., Mao, K.B., Meng, F., Shi, J.C., Zeng, J.Y., Shen, X.Y., Cui, Y.K., Jiang, L.M., Guo, Z.H., 2021. SMC dataset: soil Moisture in China dataset (2002–2018). National Tibetan Plateau/Third Pole Environment Data Center. https://doi.org/10.5281/zenodo.4738556.

Yan, G., Zhang, H., Guo, Q., Wang, X., Long, Y., 2009. Wind erosion modeling of earthen artifacts. accessed 23 September 2025 Dunhuang Res. 06, 93–99. https://kns.cnki.net/kcms2/article/abstract?v=Zb3wS6iuiaPSu9CBNcs2mHpvECFoYegTIWoJHTcK2cxANms0oyfHUKLcdVC2_QkCfoUYMKlHoedAlc_Js7FlKa-B_OZ08ItNpKAKFFjYNHKVMDmKfC6T1xL0w7gvzkr3t1oj-Q2x3wiMsF4TUwjbHkf0tG5CCMnkSejwmrO6Ji118gidAHTeN2s8cgchlvFA&uniplatform=NZKPT&language=CHS.

Cheng, Y., Nathanail, P.C., 2009. Generic assessment criteria for human health risk assessment of potentially contaminated land in China. Sci. Total Environ. 408 (2), 324–339. https://doi.org/10.1016/j.scitotenv.2009.09.021.

Zhou, J., Lu, H., Yang, K., Jiang, R., Yang, Y., Wang, W., Zhang, X., 2023. Projection of China's future runoff based on the CMIP6 mid-high warming scenarios. Sci. China Earth Sci. 66 (3), 528–546. https://doi.org/10.1007/s11430-022-1055-5.